JOURNAL OF PROPULSION AND POWER
Vol. 33, No. 4, July–August 2017

End-Wall Boundary Layers and Blockages of Multistage Axial Compressors Under Different Conditions

Xinqian Zheng* and Heli Yang†
State Key Laboratory of Automotive Safety and Energy, Tsinghua University, 100084 Beijing, People's Republic of China

DOI: 10.2514/1.B36251

End-wall boundary layers and induced blockages are important factors for multistage axial compressors' performance. This paper investigates hub and shroud end-wall boundary layers, and the corresponding blockages of a five-stage axial compressor under different conditions. The results show that the hub displacement thickness increases from the front to rear stage, whereas the shroud displacement thickness remains almost the same. At the design point, the blockage increases from 2.4% for the front stage to 14.7% for the rear stage, which is dominated by the hub displacement thickness. Under different operating conditions of 100% speed, the blockage is almost the same for the front stage, but increases significantly for the rear stage from 6.0% at near choke to 22.2% at near surge. At peak-efficiency points of different rotational speeds, the blockage remains almost the same. The steady and unsteady results show almost the same trends of displacement thickness and blockage. Compared to unsteady simulations, the time consumption of steady simulations is only one-sixtieth, which can save large amounts of computational resources. Based on the results, the trends of displacement thicknesses and blockages are almost the same in a wide range of operating conditions, which indicates that the flow control in the end-wall region for the design condition would be still effective.

Nomenclature

A_{eff}	=	effective area
A_{phy}	=	physical area
B	=	blockage
c_v	=	specific heat
E	=	strain rate tensor
e	=	internal energy
F_x	=	axial component of blade force
H	=	shape parameter
I	=	unit tensor
$\dot{m}$	=	mass flow
Pr	=	Prandtl number
p	=	static pressure
R	=	radius
R_g	=	gas constant
T	=	static temperature
$\boldsymbol{u}$	=	velocity
u_E	=	axial velocity at the edge of the boundary layer
u_x	=	axial velocity in the boundary layer
$Y+$	=	nondimensional distance from the wall
γ	=	isentropic coefficient
δ	=	boundary-layer thickness
δ^*	=	boundary-layer displacement thickness
δ_{Fx}	=	deficit thickness for the axial force
θ	=	boundary-layer momentum thicknesses
κ	=	thermal conductivity
μ	=	viscosity
π	=	pressure ratio
ρ	=	density
ρ_E	=	density in the edge of the boundary layer
ρ_x	=	density in the boundary layer
σ	=	viscous stress tensor
τ	=	tip clearance

Subscripts

h	=	hub
s	=	shroud
1	=	inlet of a blade row
2	=	outlet of a blade row

I. Introduction

THE end-wall region is an important region for compressors, including corner flow and tip-leakage flow, which ultimately influence the end-wall boundary layer (EWBL). The end-wall region has a major effect on overall performance, giving most of the losses, determining most of the blockage, and being involved in the initiation of stall [1]. Much research has been conducted to understand the flow in end-wall regions and its influence on the performance of compressors.

Early research was aimed at modeling and obtaining some empirical correlations to calculate the end-wall region. The original method to treat the EWBL is the traditional boundary-layer theory. Stratford [2] proposed a simple model to analyze the EWBL, and found that it was greatly influenced by axial blade force and axial-force deficit thickness. Despite the simplicity of the model, it shows features of the EWBL with a quantitative method. Mellor and Wood [3] developed a new theory that introduced new concepts, such as axial and tangential defect force thickness, and a rotor exit–stator inlet "jump condition," and also retained the classical parameters, such as momentum boundary-layer thickness and wall shear stress. Hirsch [4] reformulated the equation proposed by Mellor and Wood in streamline coordinates, which incorporated the shape parameter variation and the Reynolds-number effects, as well as the introduction of the wall skewing angle. De Ruyck et al. [5] introduced the transverse momentum thickness and the variation of force deficit due to tip clearance. The predicted results using the two parameters agree with experimental results. Then, De Ruyck and Hirsch [6] improved this method through the introduction of compressibility effects, an extra secondary-flow loss coefficient in the defect force assumption and profile model equations without inherent limitations and allowing jumps on the end wall. These previous models helped researchers understand the flow mechanisms in end-wall regions more clearly.

Losses in the end-wall region, which typically include EWBL loss and tip-leakage loss, are of great influence on compressor

Received 13 March 2016; revision received 22 September 2016; accepted for publication 11 October 2016; published online 30 December 2016.

*Turbomachinery Laboratory; zhengxq@tsinghua.edu.cn (Corresponding Author).
†Turbomachinery Laboratory.

performance. Denton [7] classified the losses in turbomachines into profile loss, end-wall loss, and tip-leakage loss, and the relative magnitudes of the aforementioned three categories are comparable in many turbomachines, each accounting for approximately one-third of the total loss. Koch and Smith [8] related the loss of efficiency due to the presence of end-wall effects to two parameters of an EWBL [i.e., the averaged displacement thickness (DT) and the tangential force thickness]. Denton and Pullan [9] investigated the sources of end-wall loss in axial-flow turbines, and found that the end-wall flow in the rotor is completely different from that in the stator. After identifying the loss sources in the end-wall region, some modifications for the compressor have been performed to decrease the end-wall losses. Weingold et al. [10] reduced the end-wall loss by the application of bowed stators, and substantially improved efficiency over the entire flow range. Herve et al. [11] studied end-wall losses and secondary flow in end-wall regions, and set the theoretical maximal potential for improvement techniques, such as end-wall contouring or the modification of the upstream stator. Tallman and Lakshminarayana [12,13] investigated the tip-leakage loss, and found that both the reduced tip clearance and the shroud relative motion resulted in less mass flow through the gap, a smaller leakage vortex, and less aerothermal losses.

Except for the high loss in the end-wall region, the blockage, which is mainly due to the EWBL, has great impact on pressure rise and flow range, as well as matching of multistage axial compressors. Hunter and Cumpsty [14] conducted a detailed experiment on a compressor rotor. The downstream blockage was found to increase as the rotor loading was increased, which showed that tip clearance had a deleterious effect on the performance of the compressor. Khalid et al. [15] presented a developed method that allows predictions of end-wall blockage associated with variations in tip clearance, blade stagger angle, inlet boundary-layer thickness, loading level, loading profile, solidity, and clearance jet total pressure. Their results also indicated that the loss in total pressure in the end-wall region resulted from the interaction of the leakage and passage flows. Suder [16] undertook a detailed experimental investigation to understand and quantify the development of blockage in the flowfield of a transonic, axial-flow compressor rotor (NASA Rotor 37), and discussed the impact of the shock on the blockage development, pertaining to both the shock/boundary-layer interactions and the shock/tip-leakage-flow interactions. Cumpsty [17] tested a small four-stage compressor, and suggested that it is tip clearance that is most potent in determining boundary-layer integral thicknesses and blockage. Gümmer et al. [18] presented results of numerical investigations performed to explore the benefit of EWBL removal from critical regions of highly loaded axial compressor blade rows. This resulted in a reduction of the local reverse flow, blockage, and losses in the respective near-shroud region. McDougall et al. [19] showed that the blockage caused by the EWBL is a crucial quantity at stall inception in axial compressors. Domercq and Escuret [20] investigated the effect of tip clearance and blockage on the matching of multistage axial compressors, as well as on the performance and stability.

It is very important to understand the EWBLs and the corresponding blockages of multistage axial compressors, especially the relationship between design and off-design operating conditions. This paper will analyze hub and shroud EWBLs, and the corresponding blockages in a five-stage axial compressor under different operating conditions, as well as different rotational speeds by steady three-dimensional computational fluid dynamics (CFD). To validate the results by steady simulation, an unsteady simulation was also conducted at design speed.

II. Numerical Method

The investigated compressor is a five-stage axial compressor with one inlet guide vane, five unshrouded rotors (R), and five cantilevered stators (S). This compressor is a commercial, high-performance multistage axial compressor. A schematic diagram of the investigated five-stage compressor is shown in Fig. 1. The clearances in rotor tip and stator hub are 0.25 mm, which are thought to be dynamic clearances, although the static values are different for different blades. In the following research, the tip clearances will be constant in each blade for the whole simulations. The tip clearances are approximately $0.5 \sim 1.5\%$ blade span from first stage to the last stage. Some key features of the compressor at design point are shown in Table 1.

The full three-dimensional steady and unsteady simulations are performed. The fluid is considered as ideal air. The control equations of the compressible fluid are shown as follows:

$$\frac{\partial \rho}{\partial t} + \nabla \cdot (\rho \boldsymbol{u}) = 0 \tag{1}$$

$$\frac{\partial}{\partial t}(\rho \boldsymbol{u}) + \nabla \cdot (\rho \boldsymbol{u}\boldsymbol{u}) = -\nabla p + \nabla \cdot \sigma \tag{2}$$

$$\frac{\partial}{\partial t}\left[\rho\left(e + \frac{1}{2}\boldsymbol{u}^2\right)\right] + \nabla \cdot \left[\rho\left(e + \frac{1}{2}\boldsymbol{u}^2\right)\boldsymbol{u}\right] = -\nabla \cdot (p\boldsymbol{u}) + \nabla \cdot (\sigma \cdot \boldsymbol{u}) + \nabla \cdot (\kappa \nabla T) \tag{3}$$

in which ρ is density, $\boldsymbol{u}$ is velocity, p is static pressure, σ is viscous stress tensor, e is internal energy, κ is thermal conductivity, and T is static temperature. To make the equation closed, some other equations should be added:

$$\sigma = -\frac{2}{3}\mu(\nabla \cdot \boldsymbol{u})I + 2\mu E, \qquad E = \frac{1}{2}[\nabla \boldsymbol{u} + (\nabla \boldsymbol{u})^T] \tag{4}$$

$$p = \rho R_g T, \qquad e = c_v T \tag{5}$$

$$\mu = \text{constant}, \quad \kappa = \text{constant}, \quad c_v = \text{constant}, \quad \gamma = \text{constant} \tag{6}$$

in which μ is the viscosity, I is the unit tensor, E is the strain rate tensor, R_g is the gas constant, c_v is the specific heat, and γ is the isentropic coefficient.

The structured meshes are created with H-type grids in the passage and O-type grids around the blade, which is shown in Fig. 2. There are 30 radial grid points in clearance to adequately capture the tip-leakage flow. In this research, the shear-stress-transport turbulent model is used to do all the simulations, which can give better

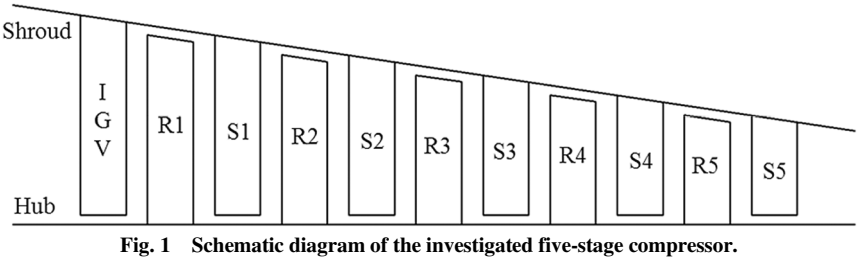

Fig. 1 Schematic diagram of the investigated five-stage compressor.

Table 1 Some key features of the investigated compressor at design point

Parameter	Value
Flow coefficient	0.55
Rotational speed	42,912 rpm
Average stage reaction	0.70
Overall pressure ratio	5.51
Stage 1 total pressure ratio	1.67
Stage 2 total pressure ratio	1.45
Stage 3 total pressure ratio	1.41
Stage 4 total pressure ratio	1.33
Stage 5 total pressure ratio	1.21
R1 inlet tip Mach number	1.50
R1 specific speed	4.98
R1 hub/tip radius ratio	0.48
R1 tip solidity	1.64

predictions in adverse-pressure-gradient flows [21]. The first element distance near the wall is set to be 0.001 mm (approximately $0.002 \sim 0.005\%$ blade span) to ensure the nondimensional distance from the wall ($Y+$) to be within 5.0. In the tip region, the $Y+$ is ensured to be less than 2.0. The inlet boundary conditions are set to be total temperature (288.15 K), total pressure (101,325 Pa), and the velocity direction (normal to the inlet). The outlet boundary condition is set as the static pressure. The solid walls are no slip and impermeable. The interface between rotor and stator is modeled as a mixing plane. The convergence criterion is set to be the root mean square less than 1.0×10^{-6}. The performance of the compressor can be obtained by increasing the outlet static pressure until the solution cannot converge.

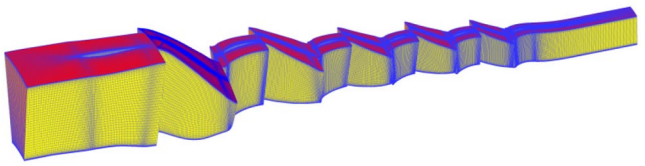

a) Whole mesh

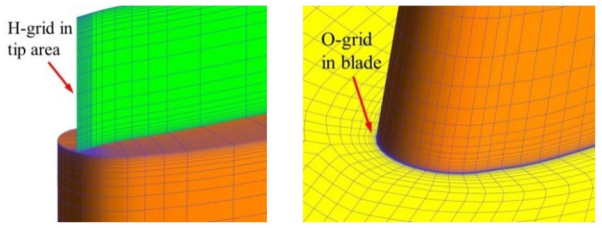

b) H-grid in tip area **c) O-grid in blade**

Fig. 2 Schematic of the grids.

Mesh independence was conducted with different mesh sizes. Different mesh sizes from 1 million elements to 9 million elements were used to calculate the performance maps, which are shown in Fig. 3. The mass flow and pressure ratio in Fig. 3 are normalized by the choked mass flow and peak pressure ratio of 7-million-element mesh, respectively. It can be observed that, as the mesh size increases, the choked mass flow, peak pressure ratio, and peak efficiency (PE) also increase. After the mesh size reaches 7 million elements, the performance remains almost the same within an error approximately 0.05%. Considering both computational capability and accuracy, the mesh size is selected to be 7 million elements.

To further validate the numerical method and the reliability of the mixing-plane method in steady simulation, an experiment was implemented with the investigated compressor. A schematic of the test facility is shown in Fig. 4. The compressor is driven by a motor to change the rotational speed. Followed with is the plenum to stabilize the pressure. By regulating the throttle at the outlet of the plenum, the performance of the investigated compressor can be obtained. The mass flow rate is measured by the flowmeter after the throttle. Total and static pressure, temperature at the inlet and outlet of the compressor, mass flow rate, rotational speed, ambient pressure, and ambient temperature were measured during the experiment. The pressure was measured by diaphragm pressure sensors with an error of less than ± 0.35 kPa. The temperature was measured by a thermocouple with an error of less than ± 0.25 K. The mass flow rate was measured by a vortex flowmeter with a relative error within $\pm 0.5\%$. The rotational speed was measured by an electromagnetic transducer with an error within $\pm 0.25\%$. The results at the design speed are shown in Fig. 5, in which the results are corrected by the standard condition (101,325 Pa and 288.15 K, which is the same inlet condition as the numerical method) and normalized by the choked mass flow and peak pressure ratio of the experimental results. The differences between experimental and numerical results are approximately 0.1% in choked mass flow, 1.4% in peak pressure ratio, and 1.1% in PE. The differences can be mainly attributed to two reasons. First, the real clearances in the experiment may be different from 0.25 mm in CFD simulations. Second, there is heat transferred to the shroud in the experiment, whereas it is assumed adiabatic in the numerical results. Despite the differences, the numerical method was validated from the agreement of experimental and numerical results.

The radial distribution of flow parameters of Rotor 37 was calculated by the established numerical method, as shown in Fig. 6, in which the experimental and numerical results from NASA [22] are also shown for comparison. It can be observed that the calculated results by this paper agree well with both experimental and numerical

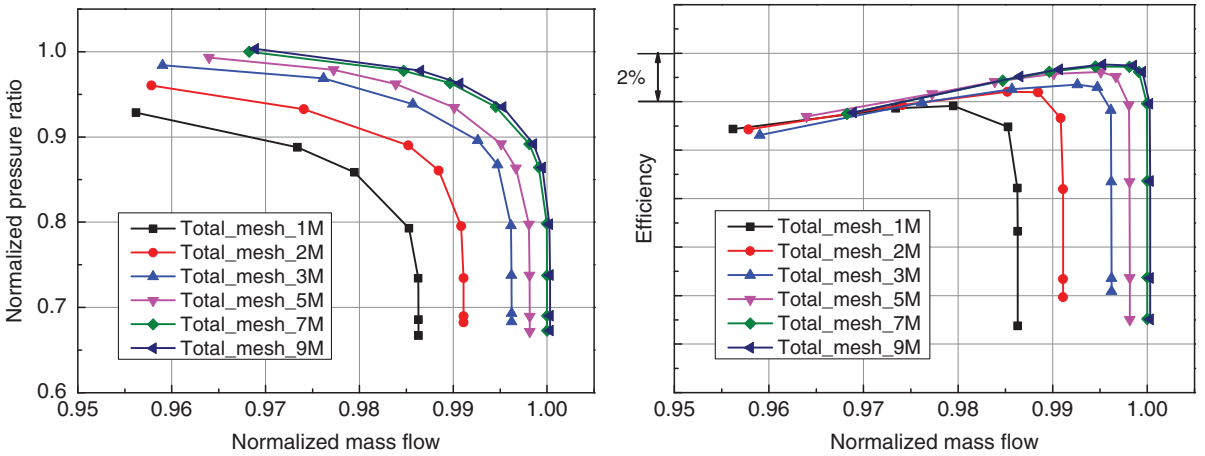

a) Pressure ratio **b) Efficiency**

Fig. 3 Map comparison of different meshes.

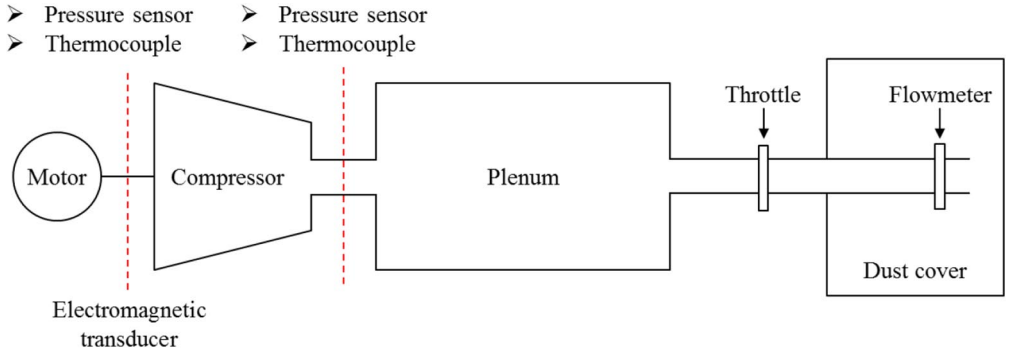

Fig. 4 Schematic of the compressor test facility.

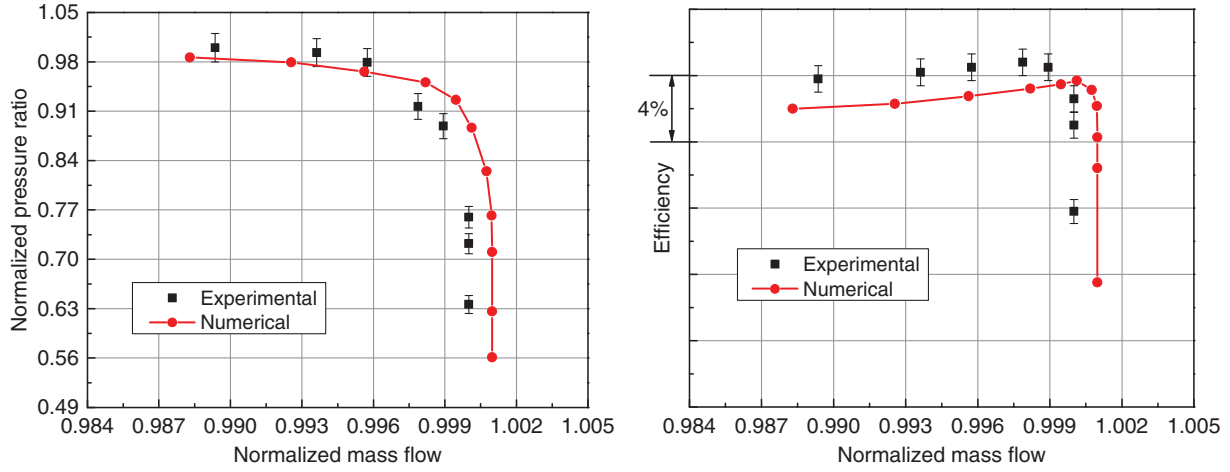

a) Pressure ratio **b) Efficiency**

Fig. 5 Comparison between experimental and numerical results of the investigated compressor at design speed.

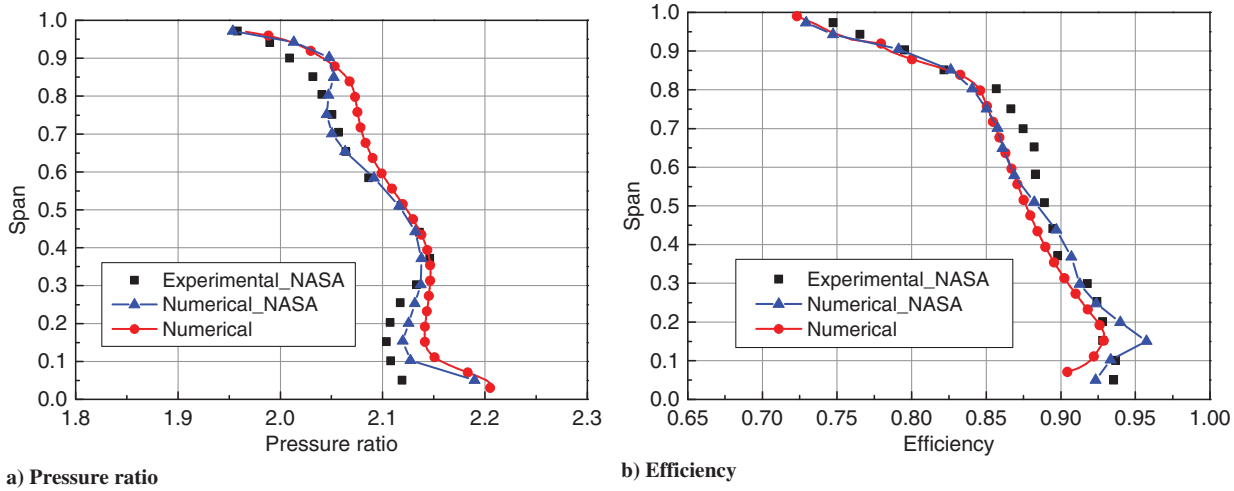

a) Pressure ratio **b) Efficiency**

Fig. 6 Radial distribution of Rotor 37.

results by NASA. This means the established numerical method can give accurate predictions in the end-wall regions. As a result, the numerical method is further validated.

III. Definitions of the EWBL and Blockage

To conveniently analyze the EWBL, many methods have been proposed to define the edge of the EWBL. Hunter and Cumpsty [14] suggested that the most convenient definition appears to be where the axial velocity either reaches a peak or reaches the uniform value of the mainstream. The latter interpretation is the method that will be employed by this paper. A typical axial-velocity profile along the span is shown in Fig. 7. Points *a* and *b* divide the whole passage into three regions: hub EWBL, mainstream, and shroud EWBL.

In multistage axial compressors, the EWBL, which grows along each surface of the annulus wall, causes a general change in the incidence of the blade, which has a great influence on its performance. The flow within the boundary layer experiences a direct change of velocity and, hence, of incidence, whereas outside the boundary layer, the velocity and incidence change because of the blockage caused by the DT. The DT or blockage thickness is a measure of the amount that the mass flow is reduced by the presence

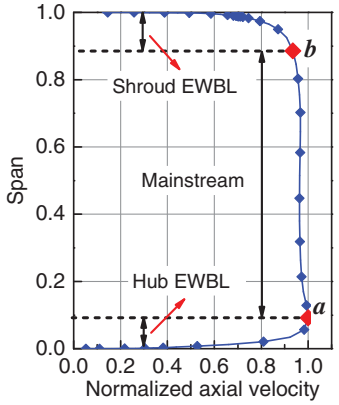

Fig. 7 Definition of EWBL based on axial-velocity profile along the span.

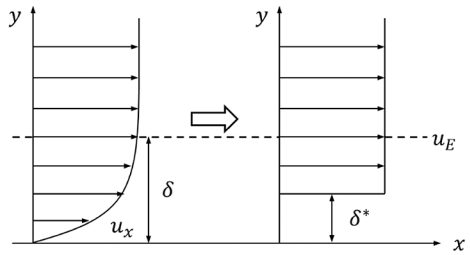

Fig. 8 Interpretation of DT.

of the EWBL from what it would be if the mainstream flow profiles were extended to the wall. A schematic for the DT is shown in Fig. 8, in which δ is the thickness of the boundary layer, δ^* is the DT, u_x is the velocity in the boundary layer, and u_E is the velocity in the edge of the boundary layer. Then, the DT can be expressed as follows:

$$\delta^* = \int_0^{\delta} \left(1 - \frac{\rho_x u_x}{\rho_E u_E}\right) \mathrm{d}y \tag{7}$$

in which ρ_x is the density in the boundary layer, and ρ_E is the density in the edge of the boundary layer.

The blockage due to the EWBL is another important parameter and is defined to show the effective area for mass flow. Figure 9 shows the interpretation of the blockage, and it can be calculated as

$$B = 1 - \frac{A_{\text{eff}}}{A_{\text{phy}}} = 1 - \frac{(R_s - \delta_s^*)^2 - (R_h + \delta_h^*)^2}{R_s^2 - R_h^2} \tag{8}$$

in which B is the blockage, A_{eff} is the effective area, A_{phy} is the physical area, R_h and R_s are the radii of the hub and shroud, and δ_h^* and δ_s^* are the DTs of the hub and shroud. With the calculated DT, the blockage can be obtained by Eq. (8). The results and analyses based on this method are shown next.

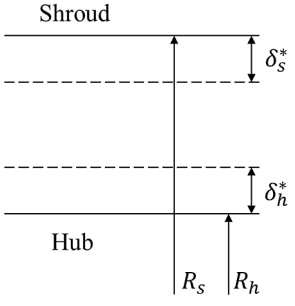

Fig. 9 Interpretation of blockage of a passage.

IV. Results and Analyses

A. Pressure Ratio and Efficiency

The performance maps of the investigated multistage axial compressor by three-dimensional steady simulation at 95, 100, and 105% of the design speed (the speeds of most concern) are shown in Fig. 10, in which the mass flow and pressure ratio are normalized by the choked mass flow and peak pressure ratio of the design speed, respectively. Points *A*, *B*, and *C* in Fig. 10 represent three typical different operating conditions: near choke (NC), PE, and near surge (NS), respectively, which are the operating points that will be analyzed in the following section of this work. The design point is the PE point of the design speed. There are also results by unsteady simulations shown in Fig. 10. Three typical operating conditions at the design speed were analyzed with unsteady simulations. The error bars of each operating condition mean the uncertainty limits of unsteady simulations, because the converged results still have some periodic fluctuations.

B. EWBLs and Blockage

1. At the Design Speed

At the design speed, the DTs of the EWBL at different operating conditions in different locations of the investigated compressors are shown in Fig. 11, in which they are normalized by the tip clearance τ. Considering the passage height of each location, the corresponding blockages calculated with Eq. (8) are shown in Fig. 12.

Figure 11 shows that the hub DT increases from the front stage to the rear stage, whereas the shroud DT keeps almost the same, but increases through a rotor and decreases through a stator, which can be observed clearly in the enlarged view of Fig. 11, as shown in Fig. 13. This is consistent with Cumpsty [17], which showed a rise in the DT across the rotor and a fall across the stator at the outer wall with the opposite occurring at the hub. The tip-leakage flow of the rotor mixes with the mainstream near-shroud end-wall region, and low-energy fluid accumulates in this region due to the tip-leakage vortex. As shown in Fig. 14, the tip-leakage vortex rolls up with the EWBL. Therefore, the EWBL becomes thickened at the rotor exit. After it flows into the stator, the mixing process continues, the fluid becomes more uniform near the shroud end wall because of the radial and circumferential redistribution of state flow variables such as pressure and temperature [23], and the DT becomes smaller, as shown in Fig. 15. However, in the hub region, the EWBL through a rotor becomes thicker because of the adverse pressure gradient. As it flows into the downstream stator, the hub leakage flow of the cantilevered stator interacts strongly with the EWBL from upstream rotor, which will thicken the hub EWBL, which can also be observed from Fig. 15 near the hub end-wall region. This is why the hub and shroud DTs show different trends. Because of the variations of DTs and the contraction of the passage from inlet to outlet, the corresponding blockages increase significantly, as shown in Fig. 12. At the PE point, the blockage increases from 2.4% for the front stage to 14.7% for the rear stage.

Figures 11 and 12 also show that the variation trends of DTs and blockages are similar with different operating conditions. However, the hub DT and blockage at NS condition are larger than that at NC condition, especially for the rear stage. From NC to NS condition, the blockage is almost the same for the front stage, whereas it increases significantly for the rear stage from 6.0% at NC condition to 22.2% at NS condition. The increase mainly comes from the increase of hub DT. A model proposed by Stratford [2] can be used to explain the aforementioned phenomena. To develop the model, the control volume around the end-wall region of a blade is given by Stratford, as shown in Fig. 16, in which u_{x1} and u_{x2} indicate the boundary-layer axial velocity at the inlet and outlet of the blade, and δ_1 and δ_2 are thicknesses of the EWBLs. Assuming that the axial velocities of the mainstream at inlet and outlet are the same, the momentum equation of the control volume can be simplified to

$$F_x \delta_{Fx} = \rho_E u_E^2 (\theta_2 - \theta_1) \tag{9}$$

in which F_x is the axial component of the blade force at the edge of the EWBL, δ_{Fx} denotes the deficit thickness for the axial force, ρ_E and u_E

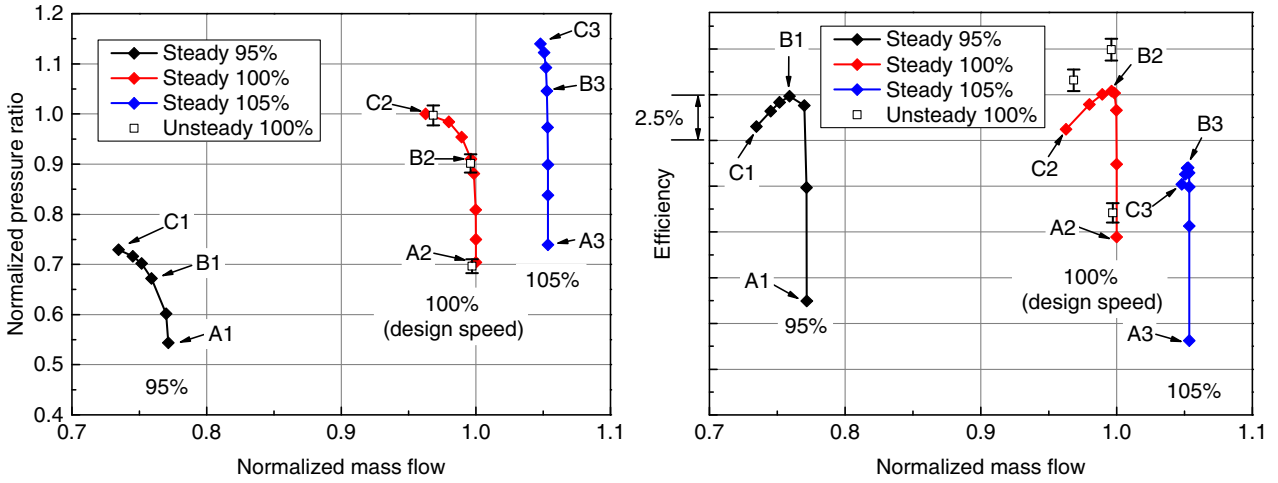

a) Pressure ratio b) Efficiency

Fig. 10 Performance map of the investigated compressor.

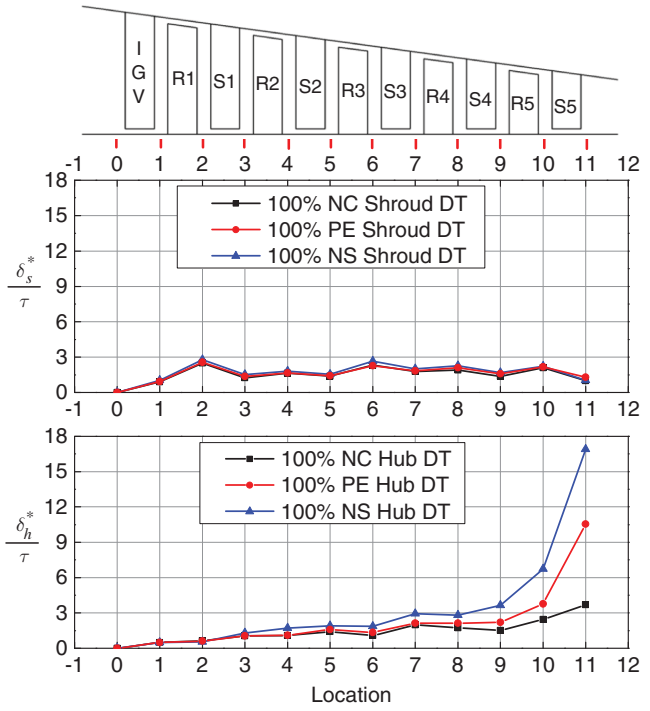

Fig. 11 EDWL DTs in different locations of the investigated compressor at design speed.

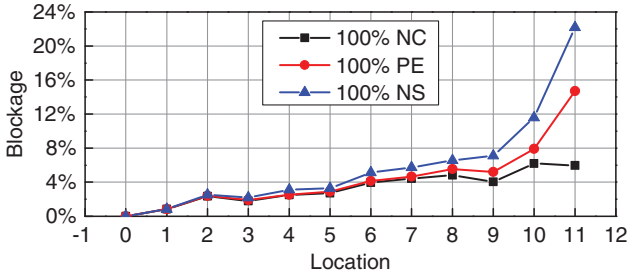

Fig. 12 Blockages in different locations of the investigated compressor at design speed.

are the density and axial velocity at the edge of the EWBL, and θ_1 and θ_2 are the momentum thicknesses of the EWBL. Consider the shape parameter, which describes the relation between θ and DT δ^*, which is always a value from 1 to approximately 2 in turbomachines [1]

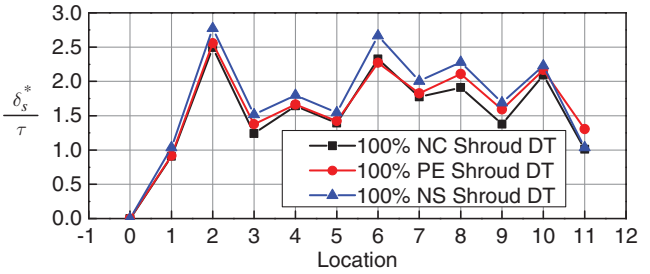

Fig. 13 Shroud DTs of different operating conditions at design speed.

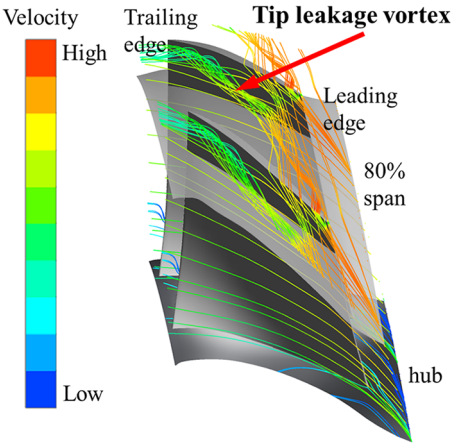

Fig. 14 Tip-leakage vortex of R1 at the design point.

$$H = \frac{\delta^*}{\theta} \tag{10}$$

Horlock and Pekins [24] took δ_{Fx} to be the product of an empirical constant K and tip clearance τ. Then, Eq. (9) can be transformed as

$$\Delta\delta^* = \delta_2^* - \delta_1^* = \frac{F_x H \delta_{Fx}}{\rho_E u_E^2} \sim \frac{F_x H K \tau}{\rho_E u_E^2} \tag{11}$$

Here, δ_1^* and δ_2^* are DTs at inlet and outlet. If F_x is somewhat proportional to the pressure rise Δp, then we get

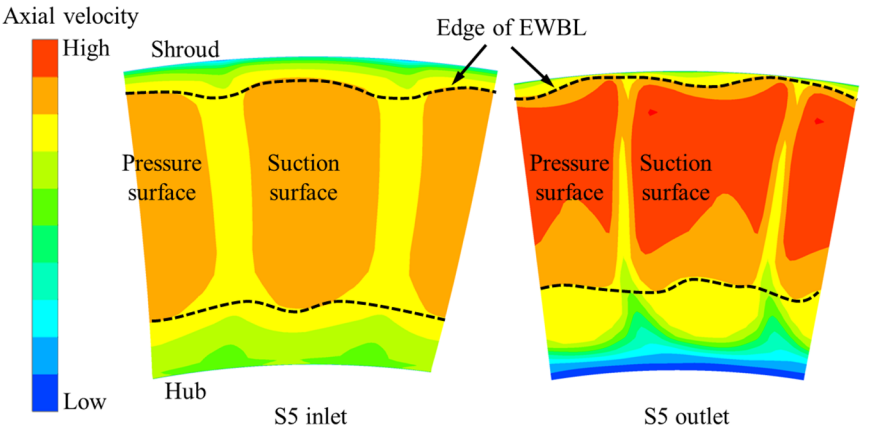

Fig. 15 Contour of axial velocity at the S5 inlet and S5 outlet.

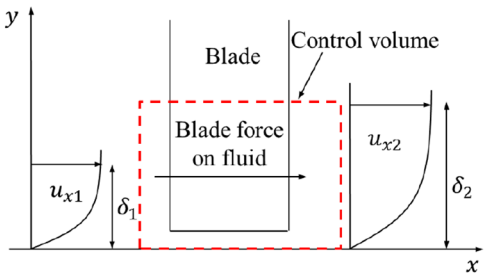

Fig. 16 Control volume around the end-wall region of a blade [2].

$$\Delta\delta^* = \delta_2^* - \delta_1^* = \frac{\Delta p}{\rho_E u_E^2} H\delta_{Fx} \sim \frac{\Delta p}{\rho_E u_E^2} HK\tau \tag{12}$$

Here, K and H vary little with different operating conditions, and τ remains constant. As it reaches the NS condition, the pressure rise Δp increases and the axial velocity u_E decreases, which leads to the increase of DT and blockage. Khalid et al. [15] and Suder [16] showed that, at NS condition, the tip-leakage flow increases due to the increase of blade loading, which also gives rise to the increase of the DT and blockage.

From Figs. 11 and 12, the differences of DTs and blockages between the NS and NC conditions at the rear stage are larger than those at the front stage. The reason of which is that the operating point varies little for the front stage, but greatly for the rear stage when the operating condition changes. Figure 17 shows the change of operating points, M and N, with different stages in typical multistage axial compressors, which indicates that, as it moves further downstream, the operating range becomes much larger. It is the amplified effect of matching that leads to larger variation of DT and blockage for the rear stage when operating conditions change [20].

Based on the analyses at the design speed, the hub region is of great importance, especially for rear stages, in which end-wall treatments (such as end bend, end bow, etc.) should be well considered while designing multistage axial compressors. The end-wall treatments can alleviate the blockage and improve the compressors' performance by changing the blade loadings and secondary flows.

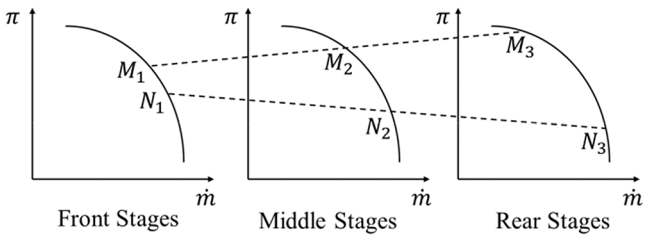

Fig. 17 Schematic for the typical matching of multistage axial compressors [20].

2. *At Off-Design Speed*

Furthermore, 95 and 105% of the design speed have also been simulated and analyzed. Figure 18 shows the DTs evolution at PE points of different rotational speeds. The overall trends agree well with different rotational speeds in spite of some small changes. The hub DTs keep almost the same with three different rotational speeds;

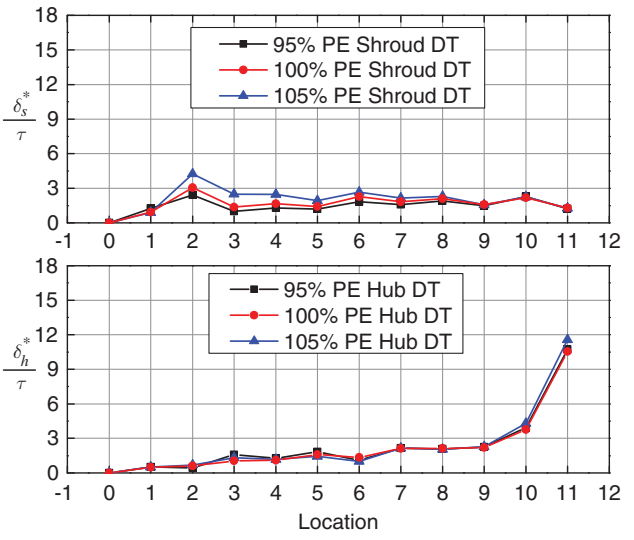

Fig. 18 DTs in different locations at PE points of different rotational speeds.

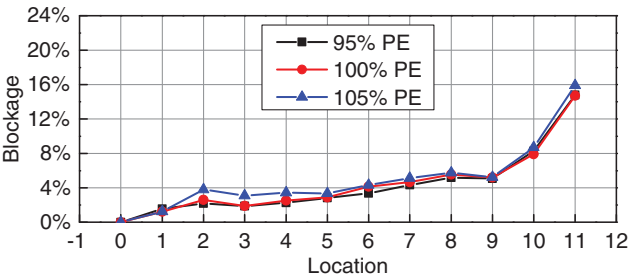

Fig. 19 Blockages in different locations at PE points of different rotational speeds.

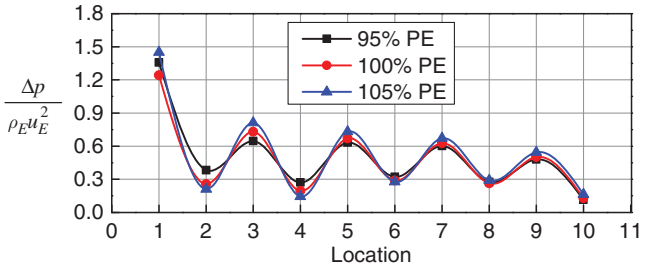

Fig. 20 Parameters $\Delta P/\rho_E u_E^2$ at different locations with different rotational speeds.

however, the shroud DTs change slightly only for front stages. The corresponding blockages are shown in Fig. 19, which shows that the blockages at different rotational speeds remain almost the same, except for the small discrepancies in front stages. From Eq. (12), the parameter $\Delta P/\rho_E u_E^2$ does not change much as the rotational speed increases, as shown in Fig. 20, because ΔP and $\rho_E u_E^2$ are both proportional to the square of the rotational speed. The shroud DTs increase slightly in the front stages when the rotational speed increases mainly because of the higher blade loading and higher Mach number, which leads to more tip-leakage flow. This also results in a stronger interaction between the tip-leakage flow and the passage shock [16]. The higher Mach number plays a key role in the blockage increase of the front stages. However, for the rear stages of the compressor, the Mach number and the tip-leakage flow have a smaller increase. As a result, the shroud DTs and the blockages of the rear stages have insignificant variations. The blockages remain the same with different rotational speeds, which indicates that the correction factor of the blockage at the design speed is also available for a range of off-design speeds.

C. Comparison Between Steady and Unsteady Simulations

To validate the results obtained by steady simulations, unsteady simulations have also been performed to compare the results. The most obvious difference between steady and unsteady simulations is the type of interface between the rotor and the stator. For steady simulations, the interface is modeled as a mixing plane. This interface circumferentially averages the fluxes and transmits the average fluxes to the downstream component. For unsteady simulations, the interface is set as a "transient rotor–stator" interface, which accounts for transient-interaction effects at a frame change interface and predicts true transient interaction of the flow between a stator and rotor passage.

At design point B2, as shown in Fig. 10, the results from steady and unsteady simulations are analyzed. Figure 21 shows the axial-velocity profile of R1 and S1 by steady and unsteady simulations,

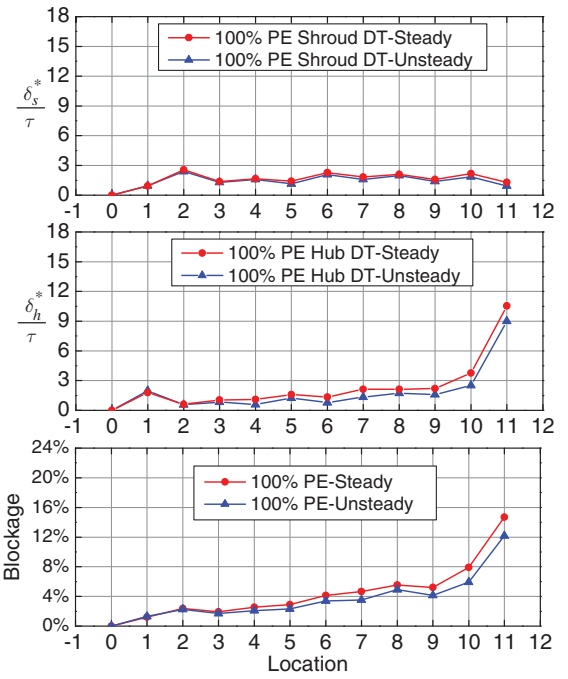

Fig. 22 Comparisons of DTs and blockages between steady and unsteady simulations.

respectively. Figure 22 shows the comparisons of DTs and blockages between steady and unsteady simulations. From Figs. 21 and 22, it can be observed that the results by steady and unsteady simulations are in good agreement. The results are almost the same for the front stages; as it moves further downstream, the differences become larger due to the different rotor–stator interface. The average difference of the blockage is approximately 0.8%. This means the steady simulation is sufficient for analyzing the EWBLs in multistage axial compressors, although the mixing-plane method is adopted by the rotor–stator interface. If this error is acceptable for designers, then a time saving approximately one-sixtieth can be achieved through the use of a steady simulation in place of an unsteady simulation.

Figure 22 also shows that the DTs and blockages of unsteady simulations are smaller than those of steady simulations, which indicates smaller loss and higher efficiency, as shown in Fig. 10. In a steady simulation, a forced mixing process can be thought to happen here due to the circumferentially averaging process downstream of the rotor–stator interface, which introduces additional entropy generation compared to that in an unsteady simulation, and results in lower efficiency.

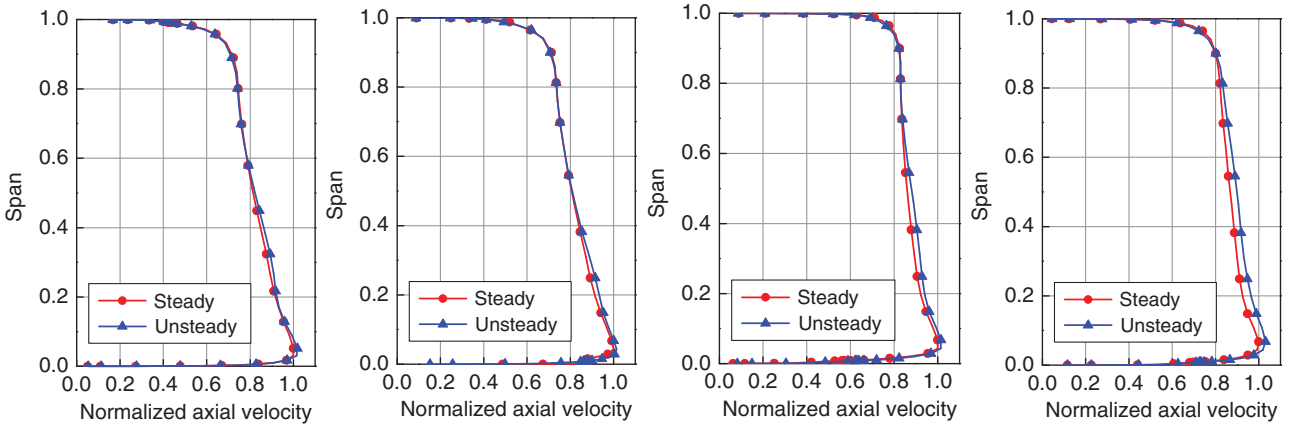

a) R1 outlet **b) S1 inlet** **c) 50% chord of S1** **d) S1 outlet**

Fig. 21 Circumferential mass-flow-averaged axial-velocity profiles of R1 and S1 by steady and unsteady simulations.

V. Conclusions

EWBLs and the blockages primarily induced by them are of great influence on the performance of multistage axial compressors, including losses, stability, and matching, especially in multistage axial compressors. The hub and shroud EWBLs and blockages of a five-stage axial compressor were studied by three-dimensional simulations. The edges of the EWBLs are defined by the axial-velocity profile along the span. Based on this definition, the DT and corresponding blockage were calculated. Different operating conditions (NC, PE, and NS) with different rotational speeds (95, 100, and 105% of the design speed) were analyzed. The conclusions could be drawn as follows.

At the design point (PE point of 100% speed), the hub DT increases from the front stage to the rear stage because of the adverse pressure gradient. However, the shroud DT remains almost the same. As a result, the blockage increases from 2.4% for the front stage to 14.7% for the rear stage, mainly due to the increase of hub DT. The end-wall effect is very important, especially for the rear stages, in which end-wall treatments (such as end bend, end bow, etc.) can be adopted to alleviate the blockage and improve the compressors' performance.

At different operating conditions of 100% speed, the variation trends of DTs and blockages from the front stage to the rear stage are similar. As it reaches NS condition, the parameter $\Delta P/\rho_E u_E^2$ increases significantly and results in the increase of blockage compared to other operating conditions, especially for the rear stage. The blockage is almost the same for the front stage, whereas it increases significantly for the rear stage, from 6.0% at NC condition to 22.2% at NS condition. The increase mainly comes from the increase of hub DT. The operating point varies less for the front stage, but larger for the rear stage because of the matching effect of multistage axial compressors.

At PE points of different rotational speeds (95 and 105% of the design speeds), the blockage of each stage remains almost the same despite small differences in the front stage. This is because the parameter $\Delta P/\rho_E u_E^2$ does not change much as the rotational speed varies. This means that the correction factor of the blockage at the design speed is also effective for a wide range of off-design speeds.

To validate the results by steady simulations with the mixing-plane method, unsteady simulations were also conducted at the design speed. The steady and unsteady results show almost the same trend of DTs and blockages with an error within 0.8%, on average. This implies that a steady simulation is sufficient for analyzing the EWBL development and blockage of multistage axial compressors. If this error is acceptable for designers, then a time saving of approximately one-sixtieth can be achieved through the use of a steady simulation in place of an unsteady simulation.

Acknowledgment

This research was supported by the National Natural Science Foundation of China (grant number 51176087).

References

[1] Cumpsty, N. A., "Flow in the Endwall Regions of Axial Compressors," *Compressor Aerodynamics*, Longman Scientific & Technical, Harlow, England, U.K., 1989, pp. 355–356.

[2] Stratford, B. S., "The Use of Boundary Layer Techniques to Calculate the Blockage from the Annulus Wall Boundary Layer in a Compressor," American Soc. of Mechanical Engineers Paper 67-WA/GT-7, Nov. 1967.

[3] Mellor, G. L., and Wood, G. M., "An Axial Compressor End-Wall Boundary Layer Theory," *Journal of Basic Engineering*, Vol. 93, No. 2, 1971, pp. 300–314. doi:10.1115/1.3425231

[4] Hirsch, C., "End-Wall Boundary Layers in Axial Compressors," *Journal of Engineering for Power*, Vol. 96, No. 4, 1974, pp. 413–426. doi:10.1115/1.3445867

[5] De Ruyck, J., Hirsch, C., and Kool, P., "An Axial Compressor End-Wall Boundary Layer Calculation Method," *Journal of Engineering for Power*, Vol. 101, No. 2, 1979, pp. 233–245. doi:10.1115/1.3446474

[6] De Ruyck, J., and Hirsch, C., "Investigations of an Axial Compressor End-Wall Boundary Layer Prediction Method," *Journal of Engineering for Power*, Vol. 103, No. 1, 1981, pp. 20–33. doi:10.1115/1.3230699

[7] Denton, J. D., "The 1993 IGTI Scholar Lecture: Loss Mechanisms in Turbomachines," *Journal of Turbomachinery*, Vol. 115, No. 4, 1993, pp. 621–656. doi:10.1115/1.2929299

[8] Koch, C. C., and Smith, L. H., "Loss Sources and Magnitudes in Axial-Flow Compressors," *Journal of Engineering for Power*, Vol. 98, No. 3, 1976, pp. 411–424. doi:10.1115/1.3446202

[9] Denton, J. D., and Pullan, G., "A Numerical Investigation into the Sources of Endwall Loss in Axial Flow Turbines," American Soc. of Mechanical Engineers Paper GT2012-69173, June 2012.

[10] Weingold, H. D., Neubert, R. J., Behlke, R. F., and Potter, G. E., "Reduction of Compressor Stator Endwall Losses Through the Use of Bowed Stators," American Soc. of Mechanical Engineers Paper 95-GT-380, June 1995.

[11] Herve, S., Reutter, O., Wieler, M., and Nicke, E., "Numerical Investigation of the Origin of Losses in the Rotor Hub Region of a Multistage Axial Compressor," American Soc. of Mechanical Engineers Paper GT2013-95013, June 2013.

[12] Tallman, J., and Lakshminarayana, B., "Numerical Simulation of Tip Leakage Flows in Axial Flow Turbines, with Emphasis on Flow Physics, Part I: Effect of Tip Clearance Height," *Journal of Turbomachinery*, Vol. 123, No. 2, 2001, pp. 314–323. doi:10.1115/1.1368881

[13] Tallman, J., and Lakshminarayana, B., "Numerical Simulation of Tip Leakage Flows in Axial Flow Turbines, with Emphasis on Flow Physics, Part II: Effect of Outer Casing Relative Motion," *Journal of Turbomachinery*, Vol. 123, No. 2, 2001, pp. 324–333. doi:10.1115/1.1369113

[14] Hunter, I. H., and Cumpsty, N. A., "Casing Wall Boundary Layer Development Through an Isolated Compressor Rotor," *Journal of Engineering for Power*, Vol. 104, No. 4, 1982, pp. 805–817. doi:10.1115/1.3227347

[15] Khalid, S. A., Khalsa, A. S., Waitz, I. A., Tan, C. S., Greitzer, E. M., Cumpsty, N. A., and Marble, F. E., "Endwall Blockage in Axial Compressors," American Soc. of Mechanical Engineers Paper 98-GT-188, June 1998.

[16] Suder, K. L., "Blockage Development in a Transonic Axial Compressor Rotor," American Soc. of Mechanical Engineers Paper 97-GT-39, June 1997.

[17] Cumpsty, N. A., "Annulus Wall Boundary Layer Measurements in a Four-Stage Compressor," *Journal of Engineering for Gas Turbines and Power*, Vol. 108, No. 1, 1986, pp. 2–6. doi:10.1115/1.3239881

[18] Gümmer, V., Goller, M., and Swoboda, M., "Numerical Investigation of End Wall Boundary Layer Removal on Highly Loaded Axial Compressor Blade Rows," *Journal of Turbomachinery*, Vol. 130, No. 1, 2008, Paper 011015. doi:10.1115/1.2749297

[19] McDougall, N. M., Cumpsty, N. A., and Hynes, T. P., "Stall Inception in Axial Compressors," *Journal of Turbomachinery*, Vol. 112, No. 1, 1990, pp. 116–123. doi:10.1115/1.2927406

[20] Domercq, O., and Escuret, J. F., "Tip Clearance Effect on High-Pressure Compressor Stage Matching," *Journal of Power and Energy*, Vol. 221, No. 6, 2007, pp. 759–767. doi:10.1243/09576509JPE468

[21] Menter, F. R., "Two-Equation Eddy-Viscosity Turbulence Models for Engineering Applications," *AIAA Journal*, Vol. 32, No. 8, 1994, pp. 1598–1605. doi:10.2514/3.12149

[22] Bruna, D., and Turner, M. G., "Isothermal Boundary Condition at Casing Applied to the Rotor 37 Transonic Axial Flow Compressor," *Journal of Turbomachinery*, Vol. 135, No. 3, 2013, Paper 034501. doi:10.1115/1.4007569

[23] Tschirner, T., Johann, E., Müller, R., and Vogeler, K., "Effects of 3D Aerofoil Tip Clearance Variation on a 4-Stage Low Speed Compressor," American Soc. of Mechanical Engineers Paper GT2006-90902, May 2006.

[24] Horlock, J. H., and Pekins, H. J., "Annulus Wall Boundary Layers in Turbomachines," AGARD-AG-185, 1974.

N. L. Key
Associate Editor